Generalized Scidar measurements at San Pedro Martir: II. Wind profiles statistics

Rémy Avila, E Carrasco, F. Ibañez, Jean Vernin, Jean-Louis Prieur, D X Cruz

Generalized Scidar Measurements at San Pedro Mártir: II. Wind Profile Statistics

R. Avila[1]

Centro de Radioastronomía y Astrofísica, Universidad Nacional Autónoma de México, Apartado Postal 3-72, Morelia, Michoacán, C.P. 58089, México

r.avila@astrosmo.unam.mx

E. Carrasco

Instituto Nacional de Astrofísica, Óptica y Electrónica, Luis Enrique Erro 1, Tonantzintla, Puebla, C.P. 72840, México

bec@inaoep.mx

F. Ibañez

Centro de Radioastronomía y Astrofísica, Universidad Nacional Autónoma de México, Apartado Postal 3-72, Morelia, Michoacán, C.P. 58089, México

J. Vernin

Laboratoire Universitaire d'Astrophysique de Nice (UMR 6525), Université de Nice Sophia Antipolis, Parc Valrose, 06108 Nice Cedex 2, France

Jean.VERNIN@unice.fr

J.-L. Prieur

UMR 5572 d'Astrophysique, Observatoire Midi-Pyrénées – CNRS, 14 Avenue Edouard Belin, 31400 Toulouse, France

prieur@ast.obs-mip.fr

D.X. Cruz

Instituto de Astronomía, Universidad Nacional Autónoma de México, Apartado Postal 70-264, Ciudad de México, D.F., C.P. 04510, México

xochitl@astroscu.unam.mx

ABSTRACT

[1]Work partly done while at Instituto de Astronomía, UNAM, México D.F., México

We present the results of monitoring the speed of optical turbulent layers in the atmosphere above San Pedro Mártir, Mexico, during 16 nights in May 2000. The data were obtained using the generalized scintillation detection and ranging technique (generalized scidar), developed at Nice University. This paper constitutes the second part of Avila et al. (2004), where the results concerning the measurements of the optical turbulence strength obtained at the same site and time were presented. The principal results of the present article are as follows. (I) The wind profiles remain stable during each night. (II) No evident correlation is found between the turbulence intensity (C_N^2) and the speed of the turbulent layers V. (III) The data only suggests a correlation between C_N^2 values greater than 5×10^{-17} m$^{-2/3}$ and V values greater than 50 m s^{-1} approximately. (IV) Layers in the first 5 km and higher up than 16 km, above sea level, are similarly slow, with median speeds of 8.6 and 9.6 m s^{-1}. (V) Between 9 and 16 km, where the jet stream takes place in some of the nights, the median wind speed is 26.0 m s^{-1}, (VI) from the simultaneous measurements of $C_N^2(h)$ and $V(h)$, we compute the temporal coherence of the turbulence layer by layer. This is the first time that such data is published. In the hypothesis of Multi-Conjugate Adaptive Optics, our measurements show that the temporal responses of three deformable mirrors conjugated on the ground, at 6 and at 13 km, above sea level, would be 28, 25 and 15 ms respectively. (VII) The vertical variation of V dominates the vertical variation of the coherence time. (VIII) Also for the first time, we compare the wind velocity profiles obtained from three different techniques: generalized scidar, NCEP/NCAR (National Center for Enviromental Prediction/National Center for Atmospheric Research) Reanalysis data, and instrumented balloons. The comparison shows excellent agreement both in the modulus and the direction of the wind velocity.

Subject headings: site testing — atmospheric effects — turbulence — instrumentation: adaptive optics — instrumentation: high angular resolution

1. Introduction

Optical-turbulence layers in the Earth atmosphere are responsible for the deformation of the incoming wavefronts in astronomical observations, which in turn degrade the angular resolution. Adaptive optical systems are aimed at fully or partially recovering of the angular resolution limited by the telescope. Current developments of such systems for existing or future telescopes involve several deformable mirrors, each optically conjugated at different altitudes. These systems are known as Multi-Conjugate Adaptive Optics (MCAO). Of particular importance is the application of MCAO for extremely large telescopes. The proper development of MCAO systems require increasingly detailed studies of the optical turbulence in the atmosphere. Apart from what concerns the turbulence outer scale, all the relevant parameters for the characterization of optical turbulence, in the context of astronomical observations, can be derived from the vertical profile of the refractive

index structure constant $C_N^2(h)$ (commonly referred as turbulence profile) and the vertical profile of the turbulence-layer velocity $\mathbf{V}(h)$[1], where h denotes altitude. For example, the Fried parameter r_0 and the isoplanatic angle θ_0 can be calculated from the integral of $C_N^2(h)$ with respect to h and the 5/3–order moment of h weighed by $C_N^2(h)$, respectively, while the wavefront coherence time τ_0 is obtained from r_0 and the 5/3–order moment of $V(h)$ weighed by $C_N^2(h)$ (Vernin & Muñoz-Tuñón 1994) (V denotes the modulus of $\mathbf{V}$). These are examples of parameters that refer to the wavefront located at the entrance pupil of the telescope. The development of MCAO needs, additionally, knowledge of the altitude and turbulence intensity of the predominant turbulence-layers and their displacement velocity, in order to determine the spatial and temporal requirements (retrieved from $C_N^2(h)$ and $\mathbf{V}(h)$) of each of the wavefront sensors and deformable mirrors in the system. Using predicting filters, like Kalman's, it is possible to configure the mirrors of a MCAO system for a given time, by (i) taking into account the corrections performed in the past and (ii) using information about the modulus and direction of the turbulent layers velocity. It would then be possible to anticipate most of the correction to be performed for a given time. This would improve the performances of MCAO, and decrease its response time. Hence wind speed and wind direction are two key parameters for operating future MCAO systems. Moreover, the selection of the sites where the next–generation ground–based telescopes are to be installed needs statistical studies of the C_N^2 and $\mathbf{V}$ profiles at those sites.

In this paper we present the results of monitoring $\mathbf{V}(h)$ at San Pedro Mártir, Baja California, Mexico, using a Generalized Scidar (GS). The instrument provides simultaneous measurements of $\mathbf{V}(h)$ and $C_N^2(h)$. The results concerning the turbulence profiles have been presented by Avila et al. (2004) (hereafter referred to as Paper I). Paper I describes some generalities about the instrument and the measurement campaign. For completeness, in § 2.1 we give the relevant information about the measurement technique and in § 2.2, a résumé of the observing campaign. The results are grouped in § 3. § 3.1 gives a data overview. In § 3.2 we present the statistics of the layer velocities in several slabs of the atmosphere. A study of the vertical profile of the coherence time is given in § 3.3. A comparison of our measurements with wind profiles obtained using instrumented balloons is shown in § 3.4. In that Section we also compare our results with wind velocity profiles obtained at different elevations from a global circulation model of the NOAA (National Oceanic and Atmospheric Administration). Finally, § 4 gives a summary and conclusions.

[1]All along the paper, symbols in bold face denote two-dimensional vectors and the same symbols in normal face correspond to the modulus of such vectors.

2. Measurements of V profiles

2.1. The GS method

The method used to measure the velocity of the turbulent layers with the GS has been extensively explained by Avila et al. (2001) and Prieur et al. (2004). We give here a very succinct summary.

The GS concept consists in taking very short-exposure images of the scintillation produced by a double star, on a virtual plane located at a distance $h_{\rm gs}$, of the order of a few kilometers, below the pupil plane ($h_{\rm gs} < 0$). The C_N^2 profile can be derived from the mean autocorrelation of those images, whereas wind-velocity profiles $\mathbf{V}(h)$ can be computed from the mean cross-correlation of images taken at times separated by a constant delay Δt. Note that the mean autocorrelation and mean cross-correlation need to be normalized by the autocorrelation of the mean image. Hereafter, we will refer to this mean-normalized cross-correlation simply as *cross-correlation*. The method is based on the following principle:

We assume that the turbulent structures are carried by the mean wind without deformation. This assumption is known as *Taylor hypothesis*, and is valid for short enough time intervals. In this case, the scintillation pattern produced by a layer at altitude h, where the mean horizontal wind velocity is $\mathbf{V}(h)$, moves on the analysis plane a distance $\mathbf{V}(h)\,\Delta t$ in a time Δt. If the source was a single star, the cross-correlation of images separated by a lapse Δt, would produce a correlation peak located at the point $\mathbf{r} = \mathbf{V}(h)\,\Delta t$, on the correlation map. By determining this position, one can deduce $\mathbf{V}(h)$ for that layer. As we use a double star, the contribution of the layer at altitude h in the cross-correlation consists of three correlation peaks, which we call a triplet: a central peak located at $\mathbf{r} = \mathbf{V}(h)\,\Delta t$ and two lateral peaks separated from the central one by $\pm\boldsymbol{\rho}H$, where H is the distance from the analysis plane to the given layer $H = h - h_{\rm gs}$ and $\boldsymbol{\rho}$ is the angular separation of the double star. The cross-correlation can be written as:

$$C_{\rm c}^{**}(\mathbf{r},\Delta t) = \int_0^\infty {\rm d}h\; C_{\rm N}^2(h) \quad \{\, a\,\mathcal{C}_{\rm c}(\mathbf{r} - \mathbf{V}(h)\Delta t, H) + b\,[\,\mathcal{C}_{\rm c}(\mathbf{r} - \mathbf{V}(h)\Delta t - \boldsymbol{\rho}H, H) + \mathcal{C}_{\rm c}(\mathbf{r} - \mathbf{V}(h)\Delta t + \boldsymbol{\rho}H, H)\,]\,\}. \tag{1}$$

$\mathcal{C}_{\rm c}$ is the theoretical cross-correlation of the scintillation produced by a layer at an altitude h and unit $C_{\rm N}^2$. It differs from the theoretical autocorrelation $\mathcal{C}$ (Prieur et al. 2004) only by an eventual temporal decorrelation of the scintillation (partial failure of Taylor hypothesis) and an eventual fluctuation of $\mathbf{V}(h)$ during the integration time. The decorrelation would make $\mathcal{C}_{\rm c}$ smaller than $\mathcal{C}$, and the fluctuation of $\mathbf{V}(h)$ would make $\mathcal{C}_{\rm c}$ smaller and wider than $\mathcal{C}$ (Caccia et al. 1987). Those effects do not affect the determination of $\mathbf{V}(h)$, as the only information needed here is the position of each correlation peak. Note that $\mathcal{C}$ takes into account the spatial filtering introduced by the detector sampling. The factors a and b are given by the magnitude difference of the two stars Δm through:

$$a = \frac{1+\alpha^2}{(1+\alpha)^2} \quad \text{and} \quad b = \frac{\alpha}{(1+\alpha)^2}, \quad \text{with} \quad \alpha = 10^{-0.4\Delta m}. \tag{2}$$

2.2. Observing Campaign

The data used in this work were obtained in May 2000, at the Observatorio Astronómico Nacional de San Pedro Mártir (OAN–SPM), Mexico, located at an altitude of 2850 m above sea level. We used the GS of the Laboratoire Universitaire d'Astrophysique de Nice, France. The instrument was installed on the 1.5-m and 2.1-m telescopes (1.5mT and 2.1mT, hereafter) during 9 and 7 nights (7–15 and 16–22 May UT), respectively.

2.3. Instrumental parameters

The concept of the GS method can be found in a number of papers (Rocca et al. 1974; Avila et al. 1997; Fuchs et al. 1998; Klückers et al. 1998; Avila et al. 2001; Prieur et al. 2001, 2004). In Paper I, the instrumental characteristics concerning the determination of $C_{\rm N}^2(h)$ were presented. Here we describe the relevant parameters for the determination of $\mathbf{V}(h)$.

The scintillation images used for the computation of the cross-correlations are the same as those used for the autocorrelations (see Paper I). The image plane is situated 3 or 4 km below the pupil plane. Images are recorded inside a 64x64 window of an intensified CCD. Each pixel covers a square area on the image plane of side Δx equal to 3.1 and 4.1 cm, for the 1.5mT and 2.1mT, respectively. The spatial filtering introduced by such pixel sizes is taken into account in the inversion process by convolving the theoretical autocorrelation by the autocorrelation of the impulse response of the camera. The exposure time of each image is 1 or 2 ms, depending on the stars magnitudes and the prevailing observing conditions. One image is obtained every 20 ms. The wavelength is centered at 0.5 μm. Two 128×128 cross-autocorrelation maps - one for a time lapse of $\Delta t = 20$ ms and another one for $\Delta t = 40$ ms - are saved on disk at time intervals that depend on the number of images used to compute the cross-correlations. Most of the time, this number was equal to 2000, which gives a mean time lag between each registration of 1.32 min. The computation of the correlations are performed in quasi real time, so that only the correlations - and not the images - are stored on disk. Table 1 of Paper I lists the double stars used as light sources.

Masciadri et al. (2002) presented an analysis of the $C_{\rm N}^2$ detectivity level for the same data as those used here. In their Fig. 12, it can be seen that $\Delta C_{\rm N}^2 \Delta h < 10^{-15}$ m$^{-1/3}$ for the 2.1mT and any of the stars used. Considering that the $C_{\rm N}^2$ profiles were resampled to an altitude resolution of $\Delta h = 500$ m, we have $\Delta C_{\rm N}^2 < 2 \times 10^{-18}$ m$^{-2/3}$ for the 2.1mT. From Eq. 1 of Masciadri et al. (2002), the $C_{\rm N}^2$ uncertainty is inversely proportional to the telescope diameter. Hence, for the 1.5mT, $\Delta C_{\rm N}^2 < 2.7 \times 10^{-18}$ m$^{-2/3}$.

The resolution $\Delta\mathbf{V}$ of the wind velocity determination is set by $\Delta\mathbf{V} = (\Delta x \sec(z))/\Delta t$, where z is the zenith angle. Table 1 gives the velocity resolution for each telescope, each Δt value and $z = 0$.

2.4. Data reduction

The method used to obtain the velocity profiles out of the cross-correlation data is based on an interactive algorithm which is extensively explained by Avila et al. (2001). Prieur et al. (2004) presented an automatic version of that algorithm. For the reduction of the data presented here, we have used primarily the interactive algorithm. Part of the data were reduced twice using the automatic algorithm, finding an excellent agreement. Here we recall the basis of the interactive algorithm.

Figure 1 shows an example of a cross-correlation map. Three horizontally aligned triplets - labeled A, B and C - can be seen. As explained in § 2.1, for a given triplet, the distance from the map center to the central peak equals $\mathbf{V}\Delta t$, which gives $\mathbf{V}$, and the distance from the central peak to either of the lateral peaks equals $\boldsymbol{\rho} H$, which gives the layer altitude h through $H = h - h_{\rm gs}$. The interactive algorithm consists in clicking with the mouse on the triplet center and on either of the lateral peaks. The program computes the layer velocity $\mathbf{V}$ and altitude h, and determines the $C_{\rm N}^2$ value from the previously obtained $C_{\rm N}^2(h)$ profile. These data are used to compute a correlation triplet and subtract it from the cross-correlation map.

Sometimes, there are several layers apparently at the same altitude, with different velocities. Our interpretation is that they are actually situated at slightly different altitudes, which cannot be resolved in the $C_{\rm N}^2$ profile. In this case, the measured $C_{\rm N}^2$ at the altitude of these layers corresponds to the sum of the real $C_{\rm N}^2$ of each layer. To determine those individual $C_{\rm N}^2$ values, the measured $C_{\rm N}^2$ is distributed to the layers at the same altitude, with weights proportional to the peak amplitudes in each of the corresponding triplets.

The dome seeing is retrieved from the cross-correlation maps. When at least two triplets are detected at the observatory altitude and one of them has a velocity smaller than the velocity resolution, this triplet is interpreted as being generated inside the telescope dome, where the mean wind velocity is zero. The dome seeing is then retrieved as in the case of multiple layer at apparently the same altitude explained above.

3. Results and Discussions

3.1. $\mathbf{V}(h)$ Data Overview

We have been able to retrieve 3016 profiles from this observation campaign. Figure 2 shows a mosaic view of all the wind–speed profiles. It can be seen that at the observatory level, the wind is generally weak. As we have excluded the data corresponding to the dome seeing, wind values at ground level are associated to open-air turbulence.

In many cases, dots with different colors appear superimposed, which indicates the presence of several turbulent layers with altitude differences smaller than the vertical resolution of the C_N^2 profiles, but with detectable velocity differences. This feature constitutes a strong advantage of the simultaneous measurement of $C_N^2(h)$ and $\mathbf{V}(h)$ as opposed to the solely measurement of $C_N^2(h)$. The velocity of the layers represents an additional dimension in the parameter space that characterizes each layer. Therefore, the determination of each layer velocity can help to identify individual turbulent layers.

The fastest turbulent layers are found between 9 and 16 km. In this altitude range, a slow modulation of the layer speed from night to night can be noticed: during the first four nights the speed was lower than 20 m s^{-1}, then it started to increase, reaching 55 m s^{-1} on May 17 UT, and then decreased to values lower than 10 m s^{-1} on the last was generally lower than 10 m s^{-1}.

The wind–direction profiles are shown in Fig. 3. It can be seen that the wind blows predominantly from West to East (i.e. around 270°) at every altitude. In general, the wind direction varies very little as a function of altitude. However, on May 21, there was a steep variation of the wind direction at 10 km approximately that lasted all night long. The following night, the same gradient in wind direction was still present, but less pronounced.

In Fig. 4 we reproduce Figure 1 of Paper I, which represents a mosaic view of the C_N^2 profiles that were obtained using the same data as that used for the wind profiles. From a visual inspection of Figs. 2 and 4, it can be seen that only the night on May 17 UT and in the jet stream layer, an evident correlation is present between C_N^2 and speed values. This is confirmed by Fig. 5, where the C_N^2 values are plotted against the layer speed, for each layer detected in the whole campaign. Each frame corresponds to a different altitude interval. No particular correlation between the $\mathbf{V}$ and C_N^2 values is noticed, appart from the layers in the 9 to 16 km (Fig 5*c*) range having speeds higher than 50 m s^{-1}, which have particularly intense turbulence ($C_N^2 \gtrsim 5 \times 10^{-17} \mathrm{m}^{-2/3}$). Although this behavior is evident in our data set, further measurements would be required to draw a general conclusion. The observed general lack of correlation between C_N^2 and $\mathbf{V}$ might be due to the fact that the optical turbulence is triggered by vertical instabilities that take place at scales much smaller than the altitude resolution of the C_N^2 profiles obtained with the GS.

3.2. Wind Speed Profile Statistics

Using all the measured **V** profiles, we have computed the median, first and third quartiles values of the layer speed V as a function of height. We recall that the first quartile, median and third quartile, q_1, q_2 and q_3 of a distribution are such that 25, 50 and 75% of the events have values lower than q_1, q_2 and q_3, respectively. The corresponding plots are shown in Fig. 6*a*. It can be seen that the wind speed has similar low values near the ground (within the first 4 km) and above 16 km. In between, which corresponds to the jet stream zone, the wind speed increases strongly. The significance of the statistical values for each altitude is indicated by the number of measurements used in the computation, *i.e.* the number of detected layers, shown in Fig. 6*b*.

A more complete statistical description of the wind speed values is obtained from their cumulative distribution function (CDF), which corresponds for each value of V, to the probability of occurrence of such a value or a lower one. We computed one CDF for the wind values grouped in each of four altitude intervals: 2-4, 4-9, 9-16 and 16-25 km above sea level, as shown in Fig. 7. We can see, for example, that 10% of the V values are lower than 3, 2, 10 and 5 m s^{-1} in the 2-4, 4-9, 9-16 and 16-25 km slabs, respectively, and 10% of the values are higher than 15, 28, 40 and 21 m s^{-1}. These numbers characterize the extreme wind conditions at each altitude interval.

3.3. Coherence Time Profiles

From the C_N^2 and **V** values of each detected layer, the coherence time τ of the wavefront deformations produced by that layer can be calculated:

$$\tau = 0.31 \frac{r_{0_{\rm ind}}}{V}, \tag{3}$$

where $r_{0_{\rm ind}}$ corresponds to the Fried's parameter that would occur if only the given layer was present:

$$r_{0_{\rm ind}} = \left[0.423 \left(\frac{2\pi}{\lambda} \right)^2 C_N^2 \Delta h \right]^{-3/5}, \tag{4}$$

where the wavelength $\lambda = 0.5$ μm. The value of τ for a given layer constrains the temporal frequency at which a deformable mirror (DM) should operate if it had to completely compensate the wavefront deformations introduced by that layer. We have calculated $\tau(h)$ from each C_N^2 and **V** profiles. The median, first and third quartiles of $\tau(h)$ are shown in Fig. 8. From the median C_N^2 profile measured at SPM, shown in Fig. 3*c* of Paper I, one could envisage a MCAO system constituted of three deformable mirrors conjugated at ground level, 6 km and 13 km above sea level. For such conjugation altitudes, the median value of τ would be 38, 25 and 15 ms approximately.

It is interesting to note that the variation of τ with altitude, seems to be exclusively governed by the variation of V. This is shown by the outstanding agreement between the median of $\tau(h)$,

and the median of the function

$$\tau_*(h) = 0.31 \frac{r_{0_{\rm med}}}{V(h)}, \tag{5}$$

where $r_{0_{\rm med}} = 0.91$ m, is the median value of $r_{0_{\rm ind}}$ for all altitudes and all turbulence profiles. The median profiles of $\tau(h)$ and $\tau_*(h)$ are shown in solid and dashed lines, respectively, in Fig. 8.

This is the first time that a study on τ profiles is published. It is extremely useful for the development of the next generation of adaptive optics systems.

3.4. Comparison with other measurements and data sets

The goal here is to compare three different values of the wind velocity profiles: those obtained with the GS, the wind speed measured simultaneously from instrumented balloons and the values obtained, for the same nights, from the global circulation model NCEP/NCAR (National Center for Enviromental Prediction/National Center for Atmospheric Research) Reanalysis Project. This is the first published comparison between GS and NCEP/NCAR wind profiles.

The balloons used are described by Azouit & Vernin (2005). The wind values are retrieved from the temporal derivative of the balloon horizontal position.

The NCEP/NCAR Reanalysis database model uses a state-of-the-art analysis and forecasting system to perform data assimilation using data from 1948 to the present. It is considered as one of the most reliable analysed fields (Kisler et al. 2001) as it is constrained by observational information such as land, marine, balloon, satellite and aircraft data. The Derived NCEP Pressure Level Product provides the 6-hourly U-wind and V-wind components of wind velocity at 17 different pressure levels.

San Pedro Mártir (SPM) geographic coordinate are $+31\overset{\circ}{.}05$ latitude and $-115\overset{\circ}{.}47$ longitude while the grid points closest to SPM coordinates are $+30\overset{\circ}{.}00$ and $-115\overset{\circ}{.}0$ respectively. We assume a standard atmosphere to associate the 17 pressure levels to altitutes e.g. 200 mb corresponds to 12 km above sea level. For each altitute, we obtained the velocity module from the U and V wind components for the 4 daily forecasted values[2]. For GS comparison purposes we average only the 6 and 12 UT wind velocity values.

3.4.1. Wind speed

The comparison of the wind speed profiles for 15 nights are shown in Fig. 9, where the date is indicated on top of each frame. The solid lines correspond to the mean speed profiles obtained each night with the GS, excluding dome turbulence. The dotted lines are the wind speeds measured with

[2]Wind blows to East and North for $U > 0$ and $V > 0$, respectively.

balloons when available. There was at most one balloon flight per night. The wind speed profiles obtained from the NCEP/NCAR Reanalysis model are shown in dashed lines. A visual comparison shows a very good agreement between the three data sets. The NCEP/NCAR Reanalysis profiles reproduce remarkably well the in situ measurements both, those from the instrumented balloons and also the GS values, excepting the features shown on 13, 14 and 15 May at about 5 km. The higher resolution of the balloon measurements shows the spatial wind speed fluctuations that could not be appreciated otherwise.

The wind direction profiles obtained with the three different methods are plotted in Fig. 10. The agreement below 20 km is generally remarkable. Above that level, the balloons measured virtually any direction. We believe that this is due to the extremely weak wind speed above 20 km.

This cross comparison brings confidence on either of the three methods for the determination of the wind speed profiles. Particularly, it indicates that for site prospection, it may suffice to determine the wind speed profile from the NCEP/NCAR Reanalysis rather than actually measure the profiles at a given site. However, for real time monitoring, the GS measurements appear to be the most adecuate method.

4. Summary and Conclusions

We presented the results of measurements of the speed and the intensity of optical turbulent layers above the Observatorio Astronómico Nacional de San Pedro Mártir, Mexico, performed with the GS, during 16 nights in May 2000. The analysis was performed on a data set where we could exclude the turbulence in the telescope dome.

The wind profiles remained fairly stable during each night. The wind speed variations occured in temporal scales of several nights.

Correlation between turbulence intensity and layer speed was only found during half a night, when very high values of both parameters were encoutered ($C_N^2 \geq 5 \times 10^{-17}$ m$^{-2/3}$ and $V \geq 50$ m s^{-1}). However, half a night of such events represents too few data to draw a definitive conclusion on the correlation of intense turbulence and fast wind.

The median wind profile shows wind velocities similarly low in the slabs that go from the ground up to 4 km and from 16 to 25 km. In between, the wind is much stronger due to the jet stream.

Using the wind and turbulence profiles, we presented the first published computation of layer-oriented temporal coherence, which is particularly useful for the development of Multiconjugate Adaptive Optics systems. It shows that the temporal responses of three hypothetical deformable mirrors conjugated on the ground, at 6 and at 13 km, above sea level, would be 28, 25 and 15 ms respectively. The vertical variation of the coherence time seems to be governed by the vertical variations of the wind profile. Such a study on the coherence time can only be obtained from

simultaneous C_N^2 and $\mathbf{V}$ profiles.

The results of this paper illustrate the usefulness of the wind velocity profile measurements performed with the GS. The consistency of those measurements with other means of wind profile determination, namely instrumented balloons and NCEP/NCAR Reanalysis, has been proved. For a virgin site, the GS is not a suitable method, as it requires a telescope of at least 1 m diameter. In that case, the NCEP/NCAR Reanalysis wind profiles are best suited. It has been shown here that NCEP/NCAR Reanalysis data can validly be used for determining both wind speed and wind direction profiles with a very good approximation. If $C_N^2(h)$ models are required, one might employ a simulation code like Meso-NH (Masciadri et al. 1999a,b, 2004). Should actual $C_N^2(h)$ and $\mathbf{V}(h)$ measurements be needed at a virgin site, a possibility is to use a Single Star SCIDAR, which is being developed at Nice University (Habbib et al. 2005).

We are grateful to the OAN–SPM staff for their valuable support. This work was done in the framework of a collaboration between the Instituto de Astronomía of the Universidad Nacional Autónoma de México and the UMR 6525 Astrophysique, Université de Nice–Sophia Antipolis (France), supported by ECOS–ANUIES grant M97U01. Funding was also provided by the grants J32412E from CONACyT, IN118199 and IN111403 from DGAPA–UNAM, and the TIM project (IA-UNAM). NCEP Reanalysis data provided by the NOAA-CIRES Climate Diagnostics Center, Boulder, Colorado, USA, from their Web site at http://www.cdc.noaa.gov/.

REFERENCES

Avila, R., Masciadri, E., Vernin, J., & Sánchez, L. 2004, PASP, 116, 682

Avila, R., Vernin, J., & Masciadri, E. 1997, Appl. Opt., 36, 7898

Avila, R., Vernin, J., & Sánchez, L. J. 2001, A&A, 369, 364

Azouit, M. & Vernin, J. 2005, PASP, 117, 536

Caccia, J. L., Azouit, M., & Vernin, J. 1987, Appl. Opt., 26, 1288

Fuchs, A., Tallon, M., & Vernin, J. 1998, PASP, 110, 86

Habbib, A., Vernin, J., & Benkhaldoun, Z. 2005, C. R. de l'Acad. Sci. Paris, 6, 385

Kisler, R., Collins, W., Saha, S., White, G., Woollen, J., Kalnay, E., Chelliah, M., Ebisuzaki, W., Kanamitsu, M., Kousky, V., van den Dool, H., Jenne, R., & Fiorino, M. 2001, Bull. Am. Meteo. Soc., 82, 247

Klückers, V. A., Wooder, N. J., Nicholls, T. W., Adcock, M. J., Munro, I., & Dainty, J. C. 1998, A&AS, 130, 141

Masciadri, E., Avila, R., & Sánchez, L. J. 2002, A&A, 382, 378

—. 2004, RevMexAA, 40, 3

Masciadri, E., Vernin, J., & Bougeault, P. 1999a, A&AS, 137, 203

—. 1999b, A&AS, 137, 185

Prieur, J. L., Avila, R., Daigne, G., & Vernin, J. 2004, PASP, 116, 778

Prieur, J.-L., Daigne, G., & Avila, R. 2001, A&A, 371, 366

Rocca, A., Roddier, F., & Vernin, J. 1974, J. Opt. Soc. Am. A, 64, 1000

Vernin, J. & Muñoz-Tuñón, C. 1994, A&A, 284, 311

Table 1. Velocity Resolution

Δt (ms)	ΔV (m s^{-1})	
	1.5mT	2.1mT
20	1.55	2.05
40	0.77	1.02

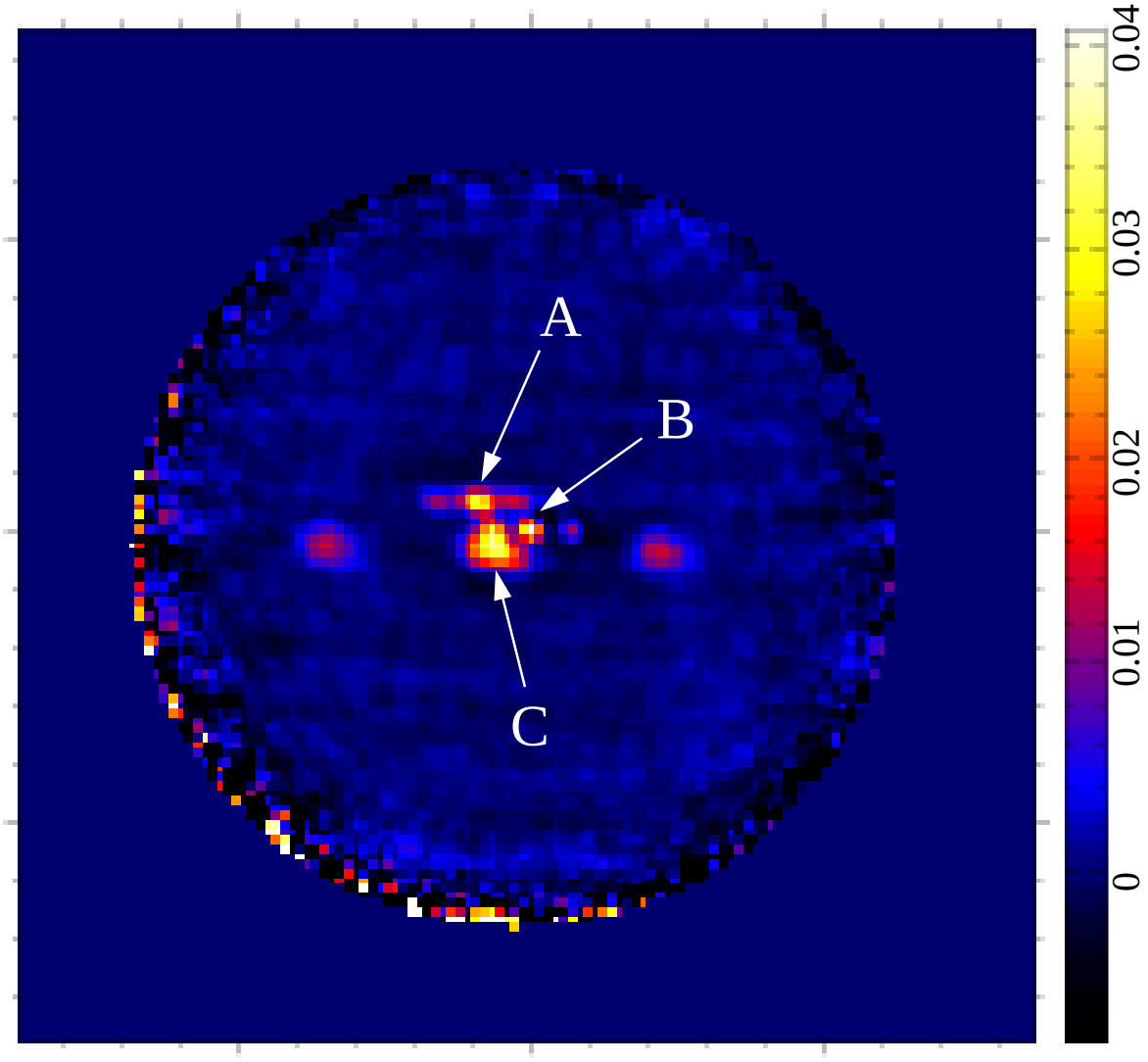

Fig. 1.— Example of a mean cross-correlation. The data were obtained with 2000 scintillation images of the 6.″4 separation double star ζ Cbr, a lag between correlated images of $\Delta t = 20$ ms and the analysis plane conjugated at $h_{\rm gs} = -4$ km. The observation was performed on 2000 May 9, 8h29 UT, at the 1.5mT. Three horizontally aligned correlation triplets can be seen - labeled A, B and C - each corresponding to a turbulent layer. The arrows point to the triplet centers. The color scale indicates normalized cross-correlation values.

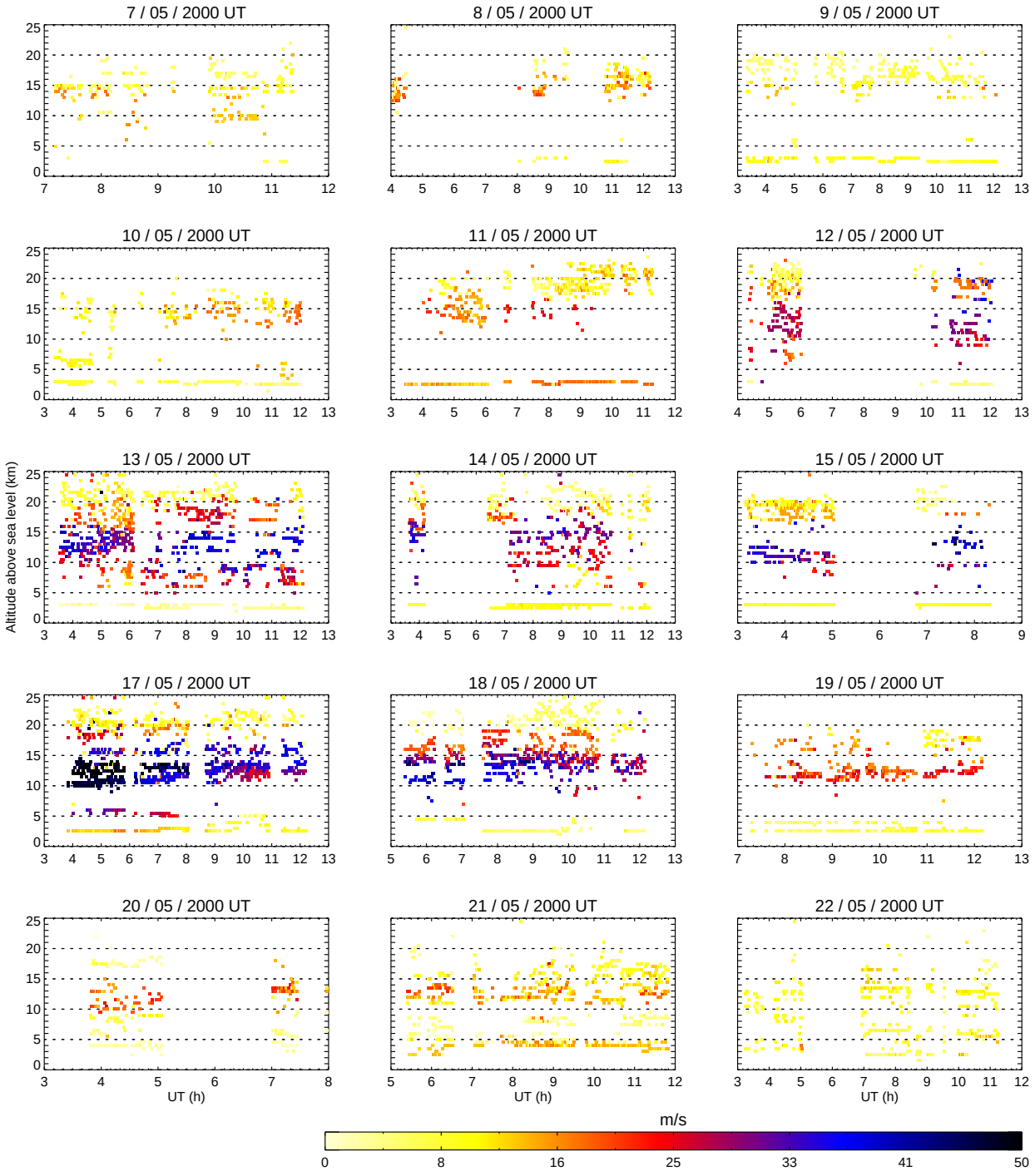

Fig. 2.— Mosaic of the wind profiles measured during the whole campaign. Each box corresponds to one night. The vertical and horizontal axes represent the altitude above sea level (observatory altitude: 2850 m) and the Universal Time, respectively. The wind speed values are coded with the color scale shown at the bottom. The three upper rows and the two bottom rows contain the profiles obtained at the 1.5mT and 2.1–mT, respectively.

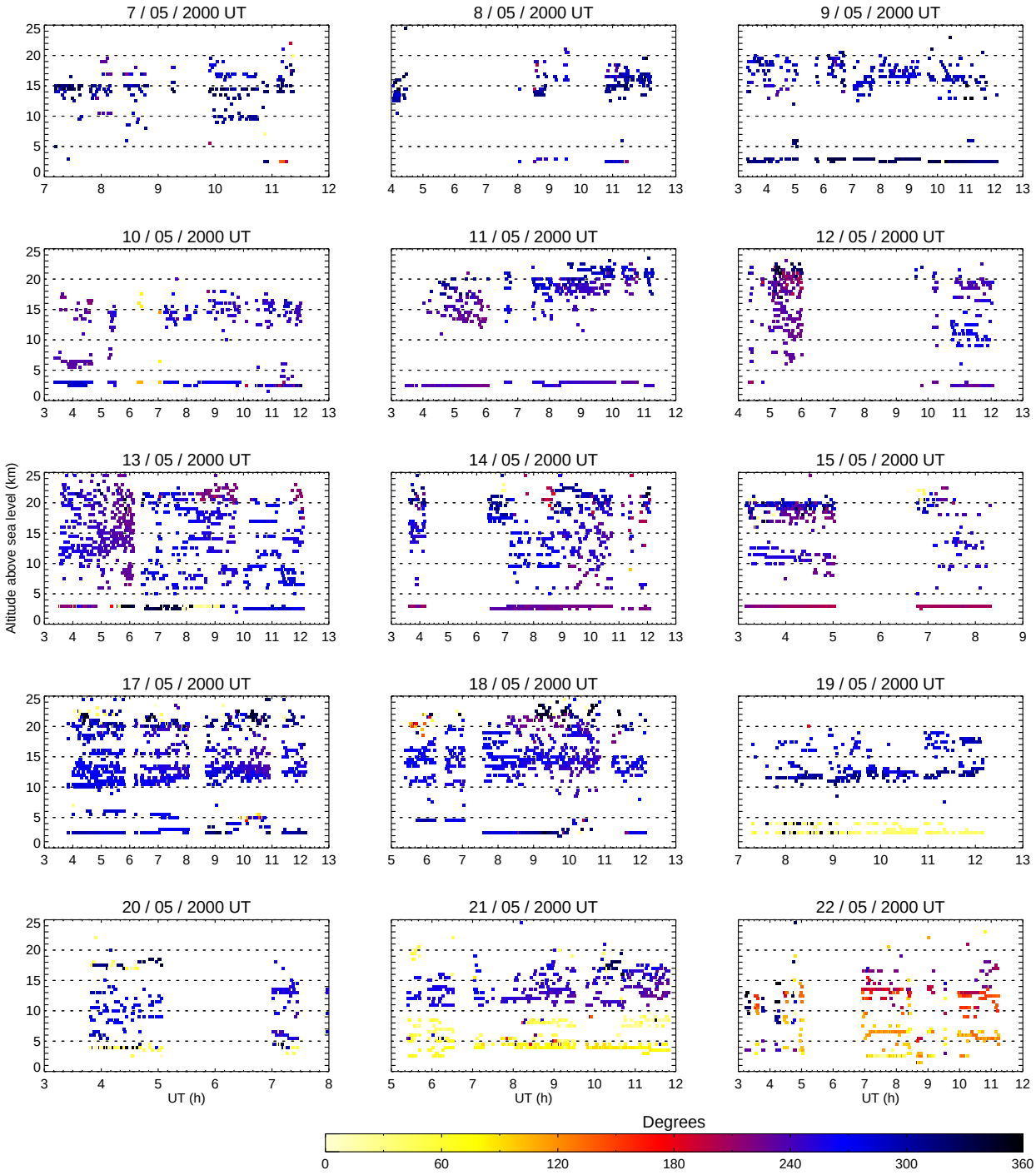

Fig. 3.— Similar to Fig. 2, but here colors represent the direction of the wind. 0°, 90°, 180° and 270° correspond to wind blowing from North, East, South and West.

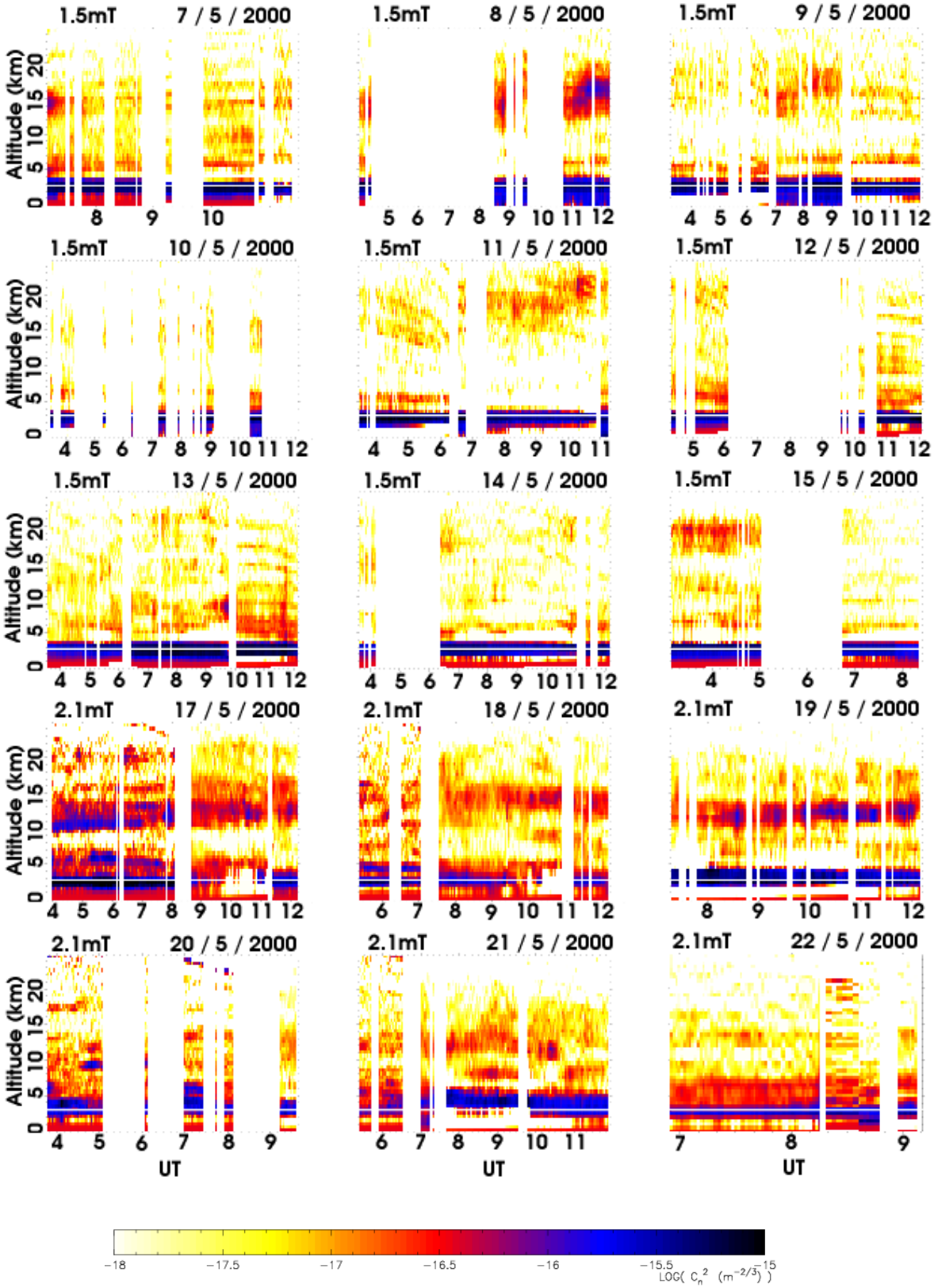

Fig. 4.— Similar to Fig. 2, but here colors represent C_N^2 values coded as shown by the logarithmic scale at the bottom.

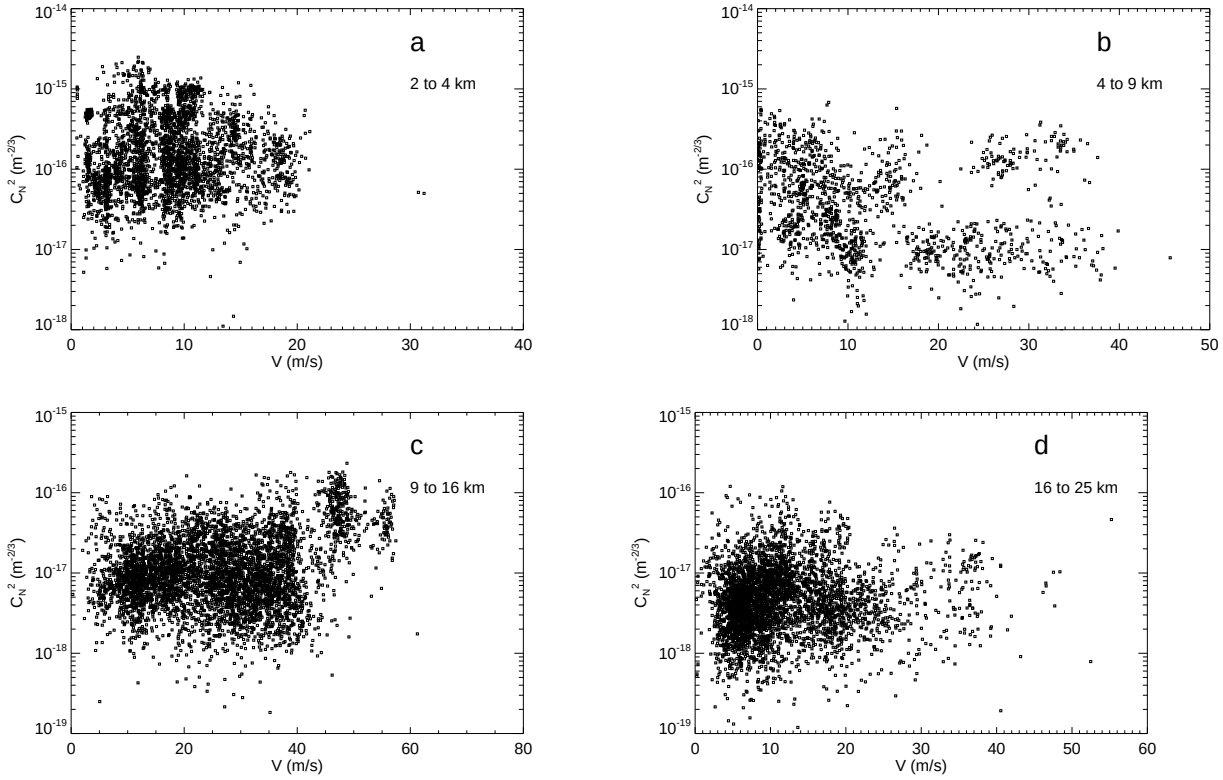

Fig. 5.— C_N^2 against **V** for all the turbulent layers detected. Each frame corresponds to a different altitude range above sea level, as indicated by the frame labels.

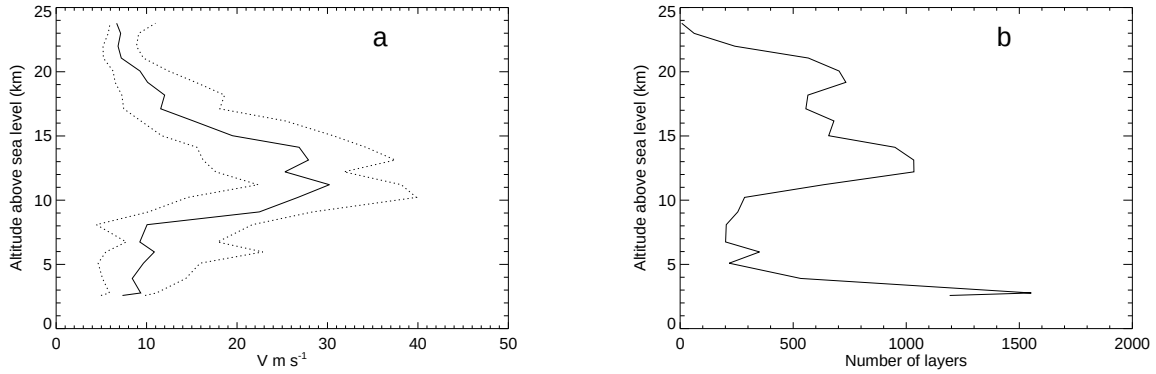

Fig. 6.— (*a*). Profiles of median (solid line), first and third quartiles (dotted lines) of the wind speed. (*b*) Profile of the number of data used for the statistical calculations. The dome-seeing layer was excluded.

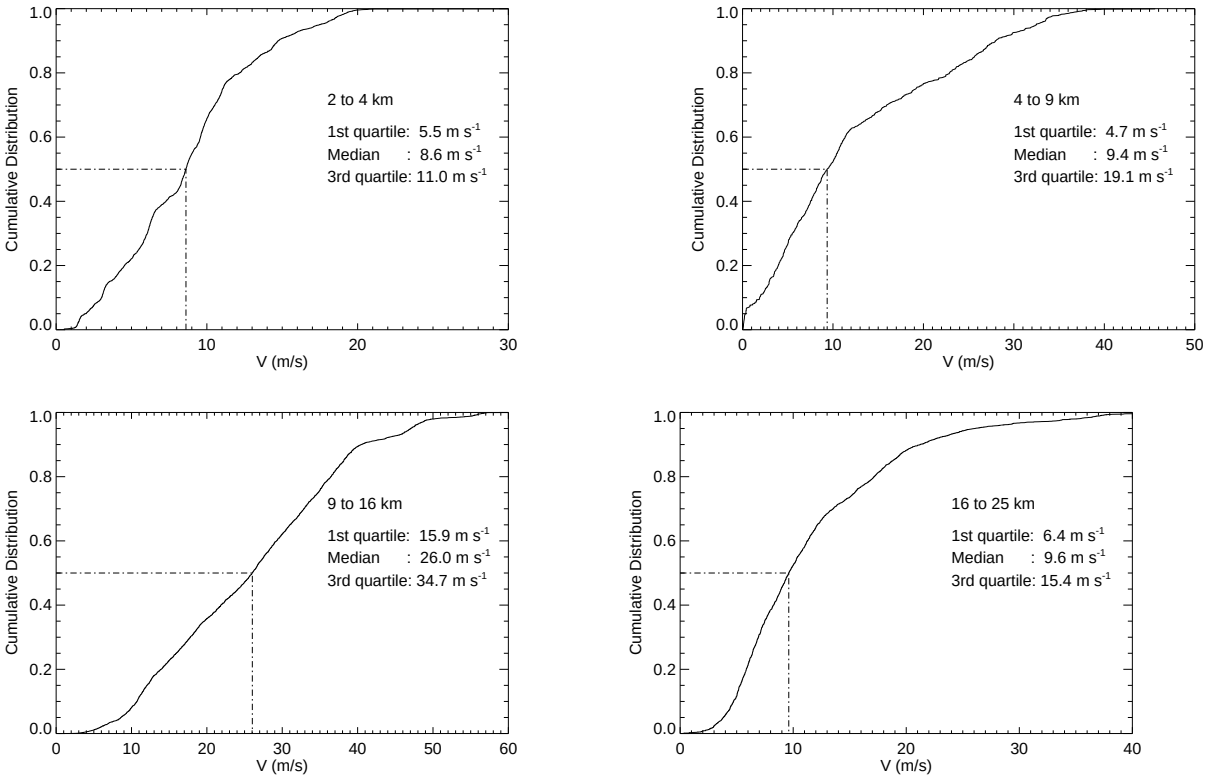

Fig. 7.— Cumulative distribution of the wind values in the altitude ranges indicated in each plot. The dome-seeing layer was excluded for the 2 to 4 altitude range.

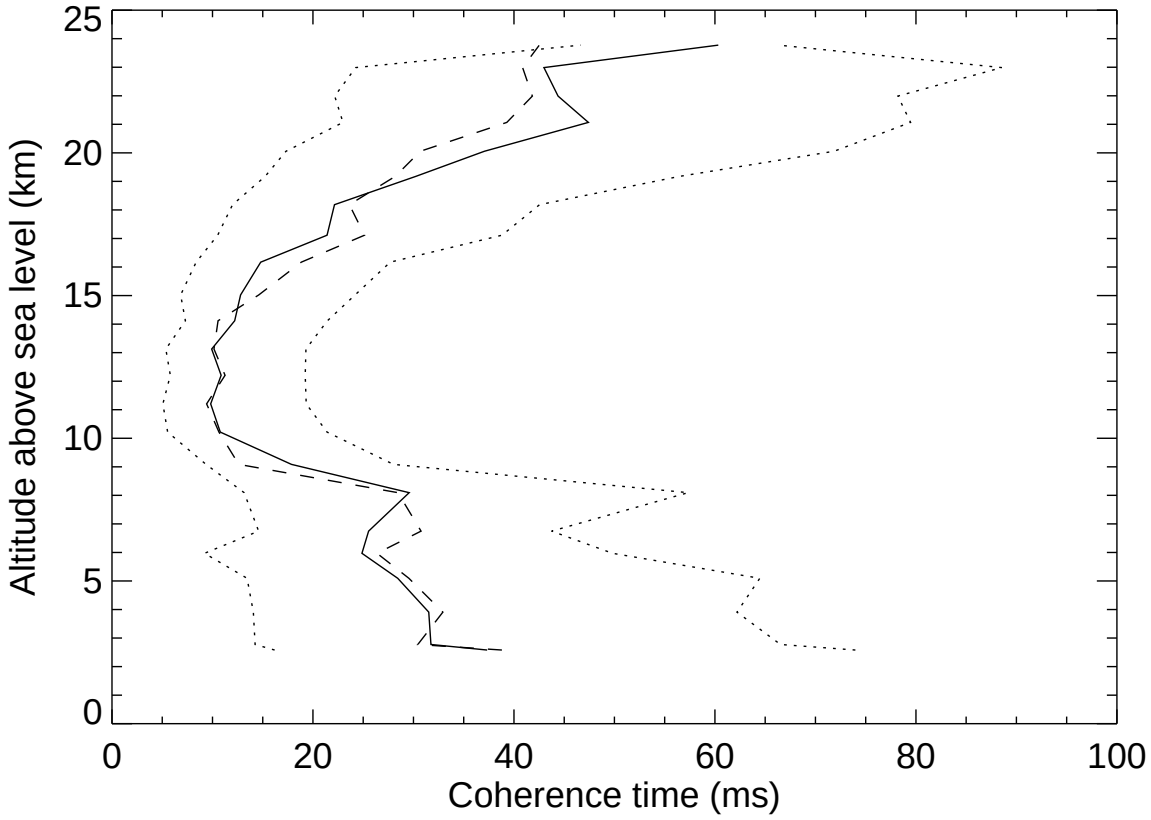

Fig. 8.— Median (solid line), 1st and 3rd quartiles (dotted lines) profiles of the coherence time for adaptive optics, as explained in the text (Eqs. 3 and 4). The dashed line represents the coherence time profile computed using Eq. 5.

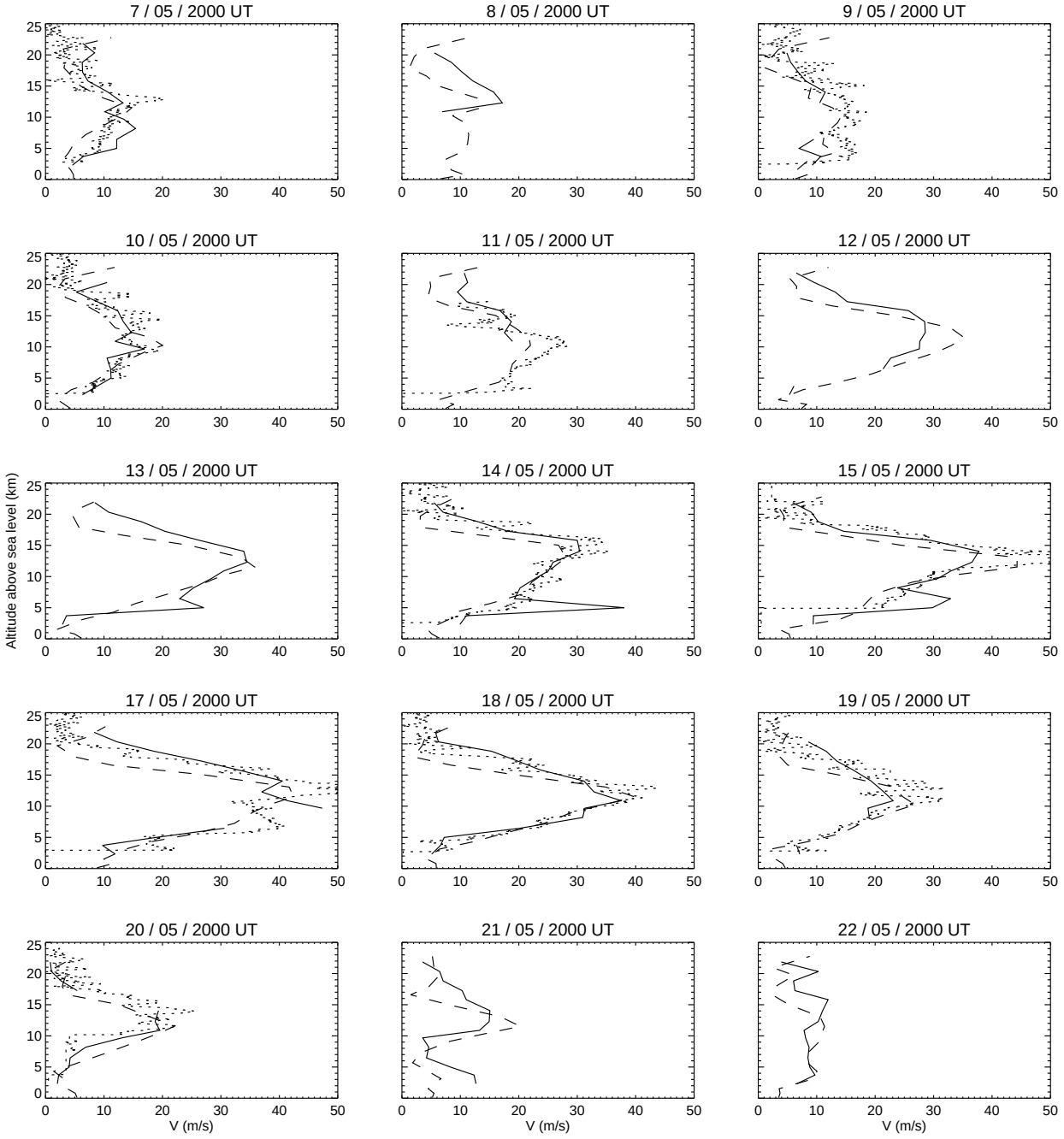

Fig. 9.— Similar to Fig. 2, but here each frame shows the mean speed profile as measured with the GS (solid lines), wind profiles obtained from the NCEP/NCAR Reanalysis project (dashed lines) and wind profiles measured with balloons (dotted lines). The GS profiles exclude dome turbulence. The NCEP/NCAR Reanalysis project profiles are the average of the 6 and 12 UT data. Each balloon profile corresponds to a single balloon launch. On some nights there was no balloon data.

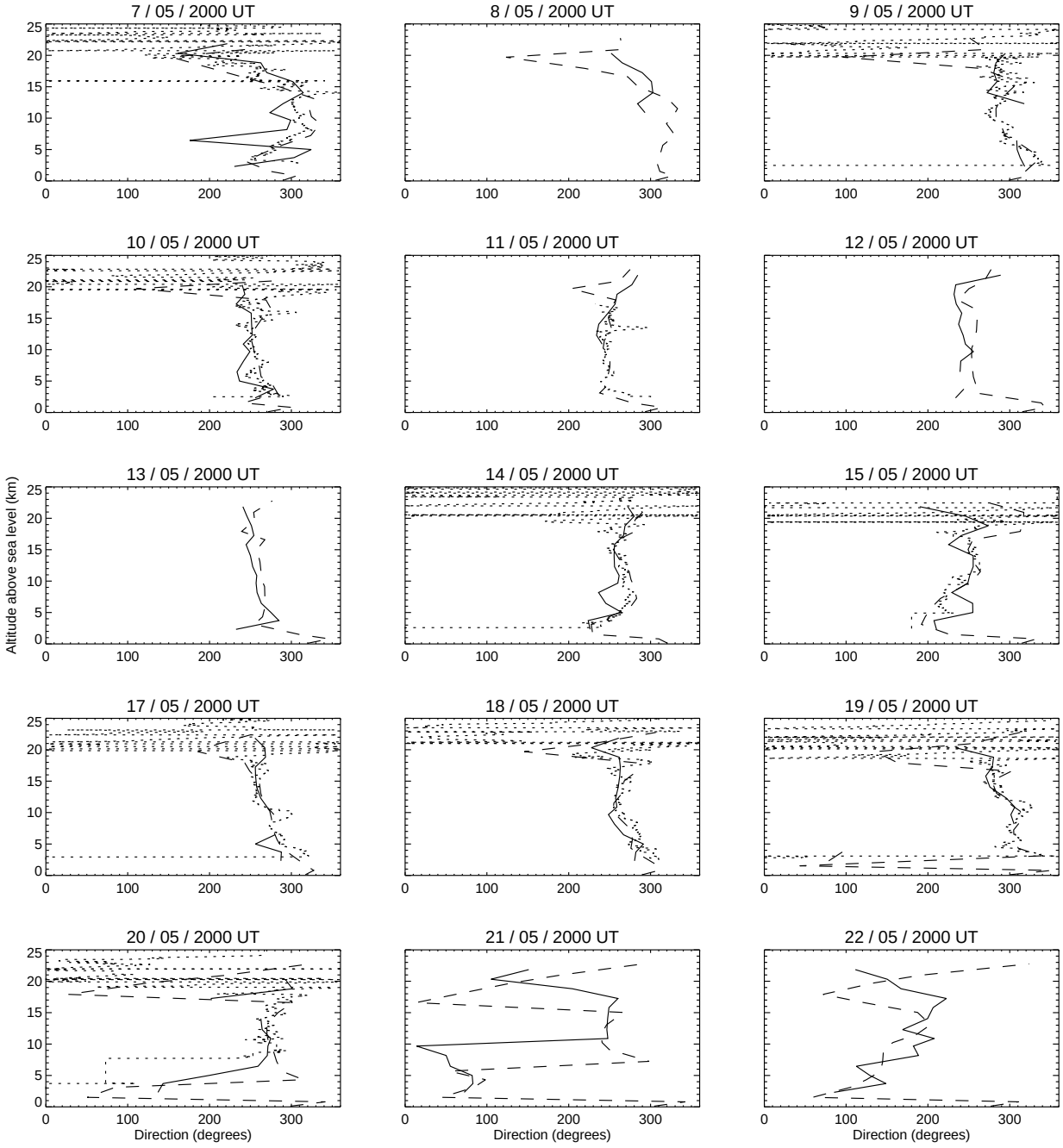

Fig. 10.— Similar to Fig. 2, but here each frame shows the wind direction profile as obtained with GS (solid lines), the NCEP/NCAR Reanalysis project (dashed lines) and those measured with the balloons (dotted lines). Wind blowing from the North, East, South and West correspond to 0, 90, 180 and 270 degrees, respectively. Like in Fig. 9, during some nights there was no balloon data.